Size Effects on Mode I and Mode II Fracture Behavior of FRP–Steel Bonded Interface
Experimental and Numerical Investigation

Yang, J.; Arouche, M. M.; Egilsson, S.; Koetsier, M.; Peeters, T.; Pavlovic, M.

Important note
To cite this publication, please use the final published version (if applicable).
Please check the document version above.

Size Effects on Mode I and Mode II Fracture Behavior of FRP–Steel Bonded Interface: Experimental and Numerical Investigation

J. Yang[1]; M. M. Arouche[2]; S. Egilsson[3]; M. Koetsier[4]; T. Peeters[5]; and M. Pavlovic, Ph.D.[6]

Abstract: Wrapped composite joints have emerged as a compelling alternative to traditional welding methods for fabricating steel circular hollow section (CHS) joints. These joints are distinguished by their superior performance in ultimate strength and fatigue resistance. This paper presents research on the interfacial properties and fracture mechanisms between fiber-reinforced polymer (FRP) and steel elements within these innovative joints. Given the large-scale dimensions of the wrapped composite joints in practical engineering, the study further explores the impact of size on their interfacial behavior. To this end, FRP–steel interface specimens were fabricated at three different scales. These specimens were subjected to double cantilever beam (DCB) and four-point end notched flexure (4ENF) testing, enabling the analysis of Mode I (opening) and Mode II (in-plane shear) interfacial behaviors. Additionally, finite-element analysis (FEA) was employed to further validate the interfacial properties and fracture characterization. The outcomes from this research provide critical insights into the FRP–steel interface in these innovative joints, which is essential for their accurate modeling and design. This understanding of the interfacial properties is key to the effective implementation and scalability of wrapped composite joints in real-world engineering projects. **DOI: [10.1061/JCCOF2.CCENG-4760](https://doi.org/10.1061/JCCOF2.CCENG-4760)**. © *2025 American Society of Civil Engineers.*

Introduction

Circular hollow section (CHS) steel structures are widely used in civil construction. Conventionally, CHSs are joined by welding the tubular steel members. These connections play a critical role in load transfer within structural systems. However, welded CHSs exhibit certain disadvantages, notably their limited performance in fatigue life, owing to stress concentrations, and environmental resistance caused by high levels of corrosion. An alternative approach is required to enhance the durability and performance of CHS joints. In response, composite wrapped joints were proposed (He and Pavlovic 2022; Feng and Pavlovic 2021) for application in steel jacket supports for offshore wind turbines. This technology involves encasing the tubular members with fiber-reinforced polymer (FRP) laminates to create a bonded connection. As a result, load transfer in the composite wrapped joints is achieved through a large bonded surface, improving the fatigue performance and environmental resistance of the structure. Pilot studies (Feng et al. 2022) revealed an enhancement of the ultimate strength and fatigue resistance of these joints, distinguishing them as a practical and cost-effective alternative for various applications.

Despite the advances in developing composite wrapped joints, a significant research gap remains in understanding bond capacity and interaction between composite and steel components. The load transfer mechanism in wrapped composite joints occurs through the FRP–steel bonded interface. In addition, the performance of this connection is affected by numerous factors, such as the material selection, surface treatment of the steel, manufacturing process of the composite laminate (He et al. 2023), and operational conditions (Arouche et al. 2022). This raises the requirement of an in-depth understanding of the FRP–steel bonded joints. In particular, the fracture behavior of FRP–steel bonded joints is fundamental for design optimization and the implementation of innovative bonded structures in engineering projects.

The fracture characterization of bimaterial bonded joints has been a trending research topic. Shahverdi et al. (2014) suggested the extended global method (EGM), based on the global method (Williams 1988), to obtain the strain energy release rate of cracks in asymmetric laminates. Wang et al. (2018) investigated a method for obtaining pure Mode I fracture in bimaterial interfaces using a double cantilever beam (DCB) test. Regarding the Mode II fracture, Ouyang and Li (2009) proposed a bimaterial end notched flexure (ENF) test configuration, where the two arms have the same longitudinal strain distribution at the faying surfaces to obtain pure Mode II fracture. Jiang et al. (2021) and Feng et al. (2024) investigated the pure Mode II fracture of FRP–steel interfaces using a four-point ENF (4ENF) test. The 4ENF tests showed the advantage of a more stable crack growth between bonded surfaces. Furthermore, an analysis of design and manufacturing

[1]Postdoctoral Researcher, Dept. of Engineering Structures, Delft Univ. of Technology, Stevinweg 1, 2628CN Delft, Netherlands. Email: j.yang-4@tudelft.nl

[2]Postdoctoral Researcher, Dept. of Engineering Structures, Delft Univ. of Technology, Stevinweg 1, 2628CN Delft, Netherlands. Email: m.moreiraarouche@tudelft.nl

[3]Dept. of Engineering Structures, Delft Univ. of Technology, Stevinweg 1, 2628CN Delft, Netherlands. ORCID: https://orcid.org/0009-0004-0979-0405. Email: s.egilsson@tudelft.nl

[4]Doctoral Researcher, Dept. of Engineering Structures, Delft Univ. of Technology, Stevinweg 1, 2628CN Delft, Netherlands. ORCID: https://orcid.org/0009-0006-4430-565X. Email: m.koetsier@tudelft.nl

[5]Dept. of Engineering Structures, Delft Univ. of Technology, Stevinweg 1, 2628CN Delft, Netherlands. Email: t.peeters-1@tudelft.nl

[6]Associate Professor, Dept. of Engineering Structures, Delft Univ. of Technology, Stevinweg 1, 2628CN Delft, Netherlands (corresponding author). ORCID: https://orcid.org/0000-0003-4911-2559. Email: m.pavlovic@tudelft.nl
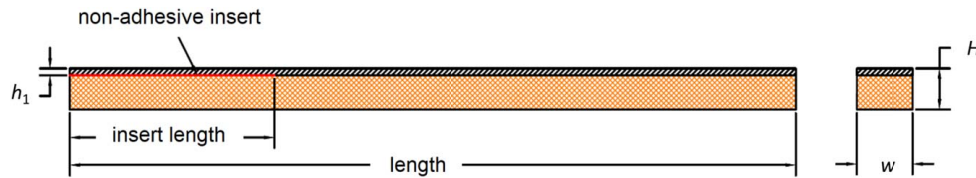
Fig. 1. FRP–steel interface specimens prepared for DCB and 4ENF tests. [Reprinted from Yang et al. (2023), under Creative Commons-BY-4.0 license (https://creativecommons.org/licenses/by/4.0/).]

parameters was made by Arouche et al. (2021a, b) using steel–composite bonded joints under mixed-mode fracture conditions. These works showed the particularities of the mechanical behavior of bonded interfaces between dissimilar materials. However, they are based on conventional coupon specimens and do not account for the geometrical implications of large-scale structural applications.

Heidari-Rarani et al. (2013) showed, by cohesive zone modeling (CZM), the effect of fiber bridging on crack development and increasing fracture toughness, in a Mode I delamination test. Numerical studies performed by Schuecker and Davidson (2000) indicated a significant effect of friction in 4ENF tests. Davidson et al. (2007) showed, by finite-element modeling, a pronounced effect of geometrical nonlinearities on the experimentally calculated fracture toughness. These works indicate a significant contribution of geometrical parameters in fracture characterization tests. In the case of bimaterial bonded joints, additional studies are needed to address the size effects on the interfacial fracture behavior.

The aim in this work is to address the gap in understanding the size effects of the mechanical behavior of steel–composite bonded interfaces for large-scale engineering structures. An experimental program was conducted to investigate the fracture behavior of FRP–steel interfaces for application in composite wrapped joints. Specimens were manufactured at three different scales: medium scale (Ms), large scale (Ls), and full scale (Fs). DCB and 4ENF tests were applied to evaluate interface fracture behavior in Mode I (opening) and Mode II (in-plane shear) loading conditions, respectively. A digital image correlation (DIC) system was implemented to measure the displacement and crack growth during the tests. Additionally, finite-element analysis (FEA) was employed to further characterize the interfacial behavior at the different sizes.

Experimental Program

Material and Interface Specimens

To support the experimental investigation, a total of 18 specimens were tested, categorized into three series in upscaling dimensions: Ms, Ls, and Fs. Each series comprised six specimens, with three designated for DCB tests and three for 4ENF tests. The interface specimens are depicted in Fig. 1, with their dimensions detailed in Table 1 for the Ms, Ls, and Fs series, respectively. Adherent 1 refers to the steel arm and Adherent 2 to the composite arm.

For the specimen manufacture, S275 steel plates of varying thicknesses—3 mm for Ms, 6 mm for Ls, and 12 mm for Fs—were selected. The yield strength of 275 MPa and the ultimate strength of 410 MPa at a strain of 0.17 were determined from three dogbone tensile tests. Before the composite lamination process, these steel plates underwent surface treatment involving grit blasting and degreasing. To create a precracked region, a nonadhesive insert with a thickness of 32 μm was positioned on the steel plate. Then, a vinyl ester resin was applied to impregnate glass fiber fabrics by hand layup lamination of the composite on the steel surface. Each composite layer consisted of a bidirectional woven fabric of glass fiber, stitched together with a layer of chopped strand glass fiber mat. After the lamination, the steel–composite plates were left to cure in ambient room conditions. The final step involved cutting the FRP–steel plates into coupon specimens, according to the predefined dimensions given in Table 1. For the bimaterial specimen configuration, the thicknesses of steel and composite adherents are designed to satisfy the principle of strain equivalence:

$$E_1 h_1^2 = E_2 h_2^2 \qquad (1)$$

where E_1 = elastic modulus of the upper arm; E_2 = elastic modulus of the lower arm; h_1 = thickness of the upper arm; and h_2 = thickness of the lower arm. This ensures that both arms of the specimens have identical longitudinal strain at their faying surfaces. Such a configuration is essential to achieve a pure-mode loading condition (Arouche et al. 2022).

It is important to note that the actual thicknesses of the specimens differ slightly from the nominal value, owing to inherent uncertainties in the manufacturing process. The material properties of steel and composite components used in this work are given in Table 2. The elastic modulus of the composite material was estimated under flexure using the composite arm of three tested specimens. The other composite material properties do not significantly affect the analysis and, therefore, nominal values were used.

Test Setup

DCB Tests

In the DCB test setup, adhesive bonds were used to attach two loading blocks to the steel and composite parts of each specimen. These blocks, were then linked to a hydraulic jack, positioned on both the upper and lower sides, using pin connections. On the specimen's

Table 1. Nominal dimensions of interface specimens in Ms, Ls, and Fs series

Parameter	Unit	Ms	Ls	Fs
Scale factor	(−)	4	2	1
Specimen length	(mm)	320	640	1,280
Insert length	(mm)	90	180	360
Steel thickness, h_1	(mm)	3.0	6.0	12.0
Specimen width, w	(mm)	25	50	100
Specimen thickness, h	(mm)	15	30	60

Table 2. Material properties of steel and composite components

Material	Elastic modulus (GPa)	Poisson's ratio (−)
Steel	$E = 210$	$\nu = 0.3$
Composite	$E_1 = E_2 = 11.8$; $E_3 = 5.7$	$\nu_{12} = 0.22$
	$G_{12} = 2.6$; $G_{13} = G_{23} = 1.8$	$\nu_{13} = \nu_{23} = 0.35$

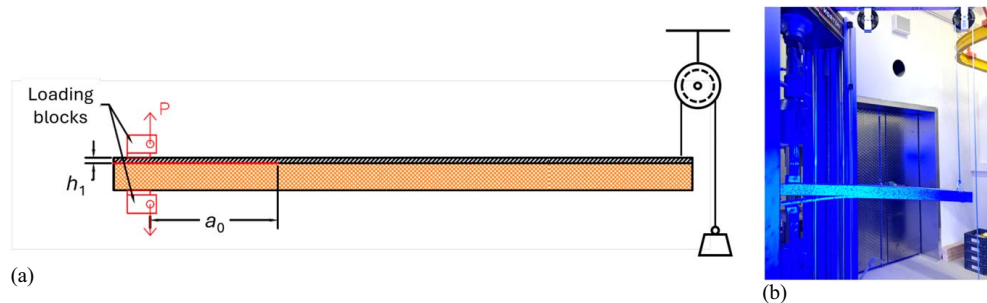**Fig. 2.** DCB interface test: (a) scheme [reprinted from Yang et al. (2023), under Creative Commons-BY-4.0 license (https://creativecommons.org/licenses/by/4.0/)]; and (b) large-scale setup [see dimensions in (Table 3)].

opposite end, a suitably weighted counterbalance was employed through a pulley system. This setup was designed to offset the self-weight of the specimen and reduce mode mixing resulting from asymmetric loading conditions. Fig. 2 depicts the DCB test configuration, with dimensions given in Table 3.

To ensure uniform loading conditions across tests, the load was applied at a constant displacement rate, of 1.0, 1.5, and 2.0 mm/min for Ms, Ls, and Fs specimens, respectively. The force exerted during these tests was measured using calibrated load cells and recorded at a frequency of 1 Hz.

4ENF Tests

Fig. 3 illustrates the setup for the 4ENF tests. Similar to the DCB tests, the 4ENF tests were conducted with the load applied at a consistent displacement rate, maintained at 1.0 mm/min for Ms specimens, 1.5 mm/min for Ls specimens, and 2.0 mm/min for Fs specimens. The applied load in these tests was also measured using calibrated load cells and recorded at a frequency of 2 Hz. The specimens were positioned consistently, with the steel arm on the top.

Measurement

The DIC technique was implemented to monitor specimen deformation in both DCB and 4ENF tests. To facilitate DIC measurements, all specimens were coated on one side with suitable white paint and sprayed with black paint to produce a random speckle pattern. A 50.6 megapixel camera was used for all scales to monitor

the crack growth during the tests. The DIC cameras were configured to capture images at a frequency of 1/5 Hz for the DCB tests and 1/3 Hz for the 4ENF tests. Additionally, polarized blue light was directed onto the specimen surface to create stable illumination for accurate measurements. The images acquired by the DIC systems were processed using the software package GOM Correlate Pro to visualize and monitor the deformation of the specimens within the measurement volume. The loads measured by the load cells were recorded, along with the image acquisition.

Experimental Results

The experimental results of the DCB and 4ENF tests were analyzed to evaluate the interfacial behaviors in Modes I and II. The load–displacement relationships were examined and compared, to provide insights into the mechanical response of the interface specimens under loading. The analysis also focused on the opening displacement occurring at the precrack tip and the propagation of the interfacial crack. To measure these parameters precisely, particularly at the interface, data acquired through DIC systems were utilized. Based on these parameters, the strain energy release rate (SERR) was determined alongside the interfacial crack evolution. The relationship between SERR and increased crack length is referred to as the R-curve, and is pivotal for evaluating the fracture toughness of the bonded interface under both Mode I and Mode II conditions.

DCB Tests

The DCB specimens at three distinct scales were analyzed to understand their interfacial properties. The upscaling in dimensions, denoted by the scaling factor, enables the impact of upscaling on these properties to be investigated. Table 4 gives the values of key parameters measured at the failure point for each specimen. In the context of this study, the failure point is defined as the stage

Table 3. Nominal dimensions of interface specimens in DCB and 4ENF test setups

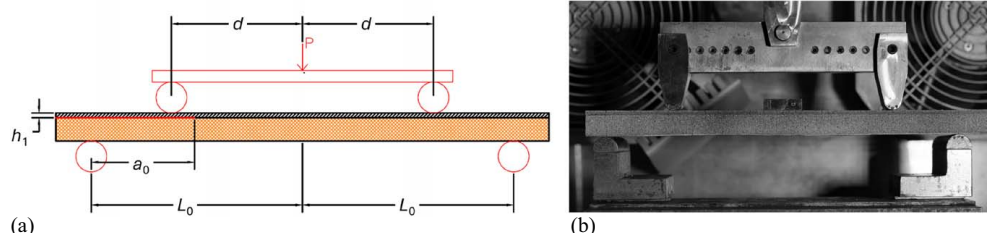| Specimen series (−)	a_0 (mm)	L_0 (mm)	D (mm)
Ms	67	137	85
Ls	134	274	170
Fs	268	548	340

**Fig. 3.** 4ENF interface test: (a) scheme [reprinted from Yang et al. (2023), under Creative Commons-BY-4.0 license (https://creativecommons.org/licenses/by/4.0/)]; and (b) midscale setup [see dimensions in (Table 3)].

Table 4. Parameters measured at the failure point of DCB specimens

Scale (−)	Specimen (−)	U_f (mm)	F_f (N)	$CTOD_f$ (mm)	Δa_f (mm)	G_1f (N/m)
Ms	Ms-DCB-401	13.7	233	1.59	10.3	0.51
	Ms-DCB-403	15	244	1.68	18.2	0.78
	Ms-DCB-405	15.4	274	1.08	13.5	0.86
Ls	Ls-DCB-01	16	955	1.61	44.2	1.77
	Ls-DCB-02	17.9	1,009	1.32	45.0	1.95
	Ls-DCB-04	16.3	973	1.66	42.9	1.7
Fs	Fs-DCB-01	24.1	2,617	3.23	56.8	1.27
	Fs-DCB-02	23.1	2,742	2.65	84.5	1.79
	Fs-DCB-03	23.3	2,949	2.29	74.4	1.98

Note: U_f = displacement; F_f = load; $CTOD_f$ = crack-tip opening displacement; Δa_f = increased crack length; and G_1f = strain energy release rate (Mode I), all at the failure point of each DCB specimen.

where the fracture process zone along the interface has fully developed. This stage is characterized by attainment of the maximum load and a noticeable increase in both the crack-tip opening displacement (CTOD) and the rate of interfacial cracking. By comparing the failure points across upscaled DCB specimens, the influence of increasing specimen size on interfacial behavior and fracture resistance can be evaluated.
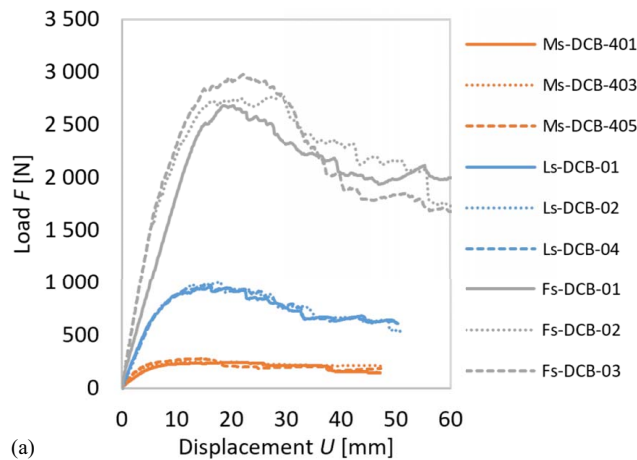
Load–Displacement

Fig. 4(a) presents the load–displacement behavior observed in the DCB specimens, providing an overview across all three scales. This figure illustrates the opening displacement occurring between the steel and composite components in response to the applied load. To measure the opening displacement precisely, DIC data were processed to exclude any deformation at the loading points. For each scale of DCB specimens, both the displacement and the load at the failure point were estimated, as given in Table 4. The mean value of failure displacement and load across different scales are depicted in Fig. 4(b). This figure exhibits a clear linear correlation between the specimen size and its mechanical response at the failure stage.

CTOD

The CTOD in Mode I measures the opening at the tip of the precrack during the tests. The CTOD is an essential parameter for characterizing the traction-separation law at the bonded interface. In this study, CTODs were obtained from DIC, which tracks the change in distance between two points that are vertically aligned with the precrack tip across the interface. The widening of the gap between these two points during the DCB tests is the CTOD. Fig. 5(a) illustrates the CTOD for DCB specimens across all three scales. For each scale, the mean CTOD at the failure point
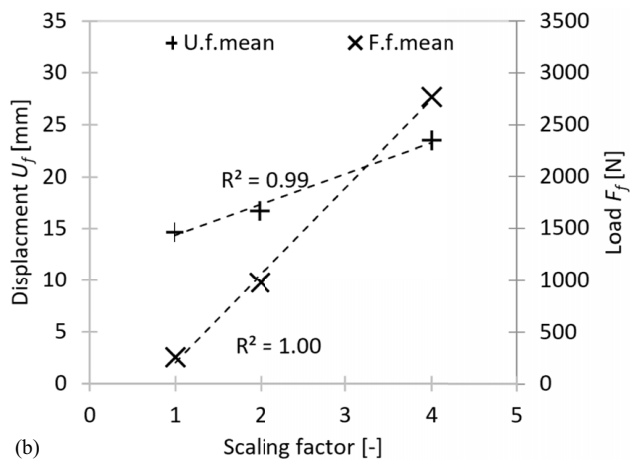

Fig. 4. (a) Load–displacement relationship of DCB specimens in Ms, Ls, and Fs series; and (b) mean values of displacement and load at failure points of DCB specimens.
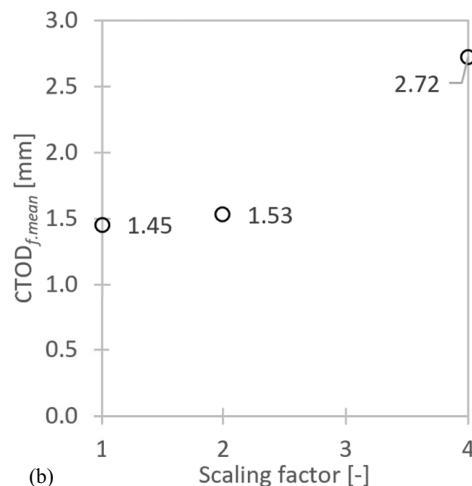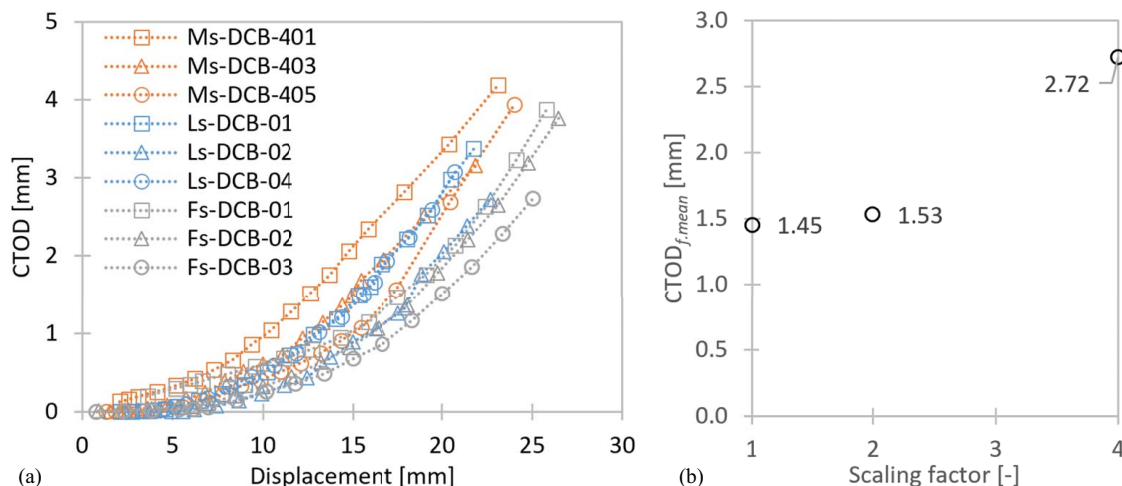

Fig. 5. (a) CTOD of DCB specimens in Ms, Ls, and Fs series; and (b) mean values of CTOD at failure points of DCB specimens.

is depicted in Fig. 5(b), which exhibits the size effect on the failure CTOD. It is important to note that the failure CTOD in Ms specimens is disproportionately larger than expected. This could be attributed to the lower bond quality at the interfaces of this batch of Ms specimens, compared with those in the Ls and Fs specimens. The suboptimal bond quality in the Ms specimens is evidenced by markedly fewer fiber bridges and reduced fracture toughness, as compared with Ls and Fs specimens. This aspect is further discussed in the subsequent section regarding R-curves in Mode I.

Development of Interfacial Cracking

The DIC technique also enables an analysis of the initiation and propagation of interfacial cracks during the loading process. Fig. 6 shows data for an Ls specimen measured by the DIC system as an example of how the interfacial crack length is determined. After postprocessing the DIC data, the opening displacement along the interface (bond line) is obtained. By setting an appropriate threshold, the crack tip could be located to determine the increased crack length for an arbitrary loading stage. A more detailed description of how crack lengths are determined can be found in He (2023, Section 4.3.4.2).

Using the DIC measurement described previously, the increased crack length in the DCB specimens was evaluated, as plotted in Fig. 7(a). The average increased crack length at the failure point for each scale of DCB specimens is displayed in Fig. 7(b). This

figure demonstrates the impact of specimen scaling on the increased crack length observed at failure. It is noteworthy that the extended crack length at failure also corresponds to the length of the fracture process zone.

R-Curves in Mode I by EGM

R-curves are instrumental in depicting the energy release characteristics of an interface during the crack propagation process. By using the EGM (Shahverdi et al. 2014), the Mode I SERR, corresponding to the estimated crack growth at each stage, was calculated:

$$\psi = \frac{(EI)_{eq2}}{(EI)_{eq1}} \tag{2}$$

$$M_1 = M_I + M_{II} \tag{3}$$

$$M_1 = M_I + M_{II} \tag{4}$$

$$G_I = \frac{M_I^2}{2B(EI)_{eq1}} \left(\frac{1+\psi}{\psi}\right) \tag{5}$$

Fig. 8(a) presents the evolution of SERR in Mode I (G_I) against the increase in crack length in the DCB specimens. Notably, the values of G_I in the Ms specimens reached an average plateau of 0.7 N/mm when the fracture process zone was fully developed.
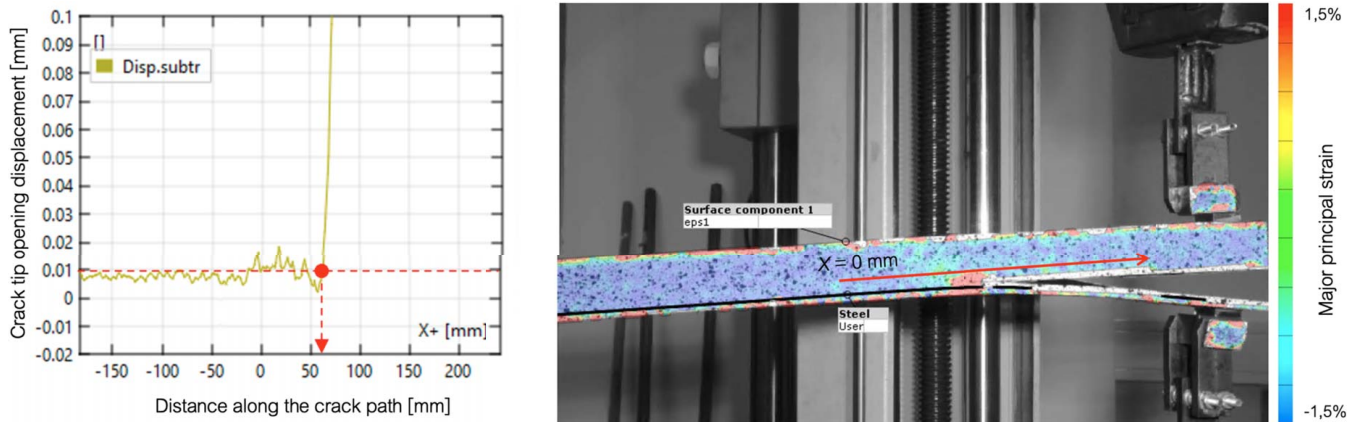

Fig. 6. Identification of location of crack tip in Ls-DCB specimen based on DIC-acquired data. [Reprinted from Yang et al. (2023), under Creative Commons-BY-4.0 license (https://creativecommons.org/licenses/by/4.0/).]
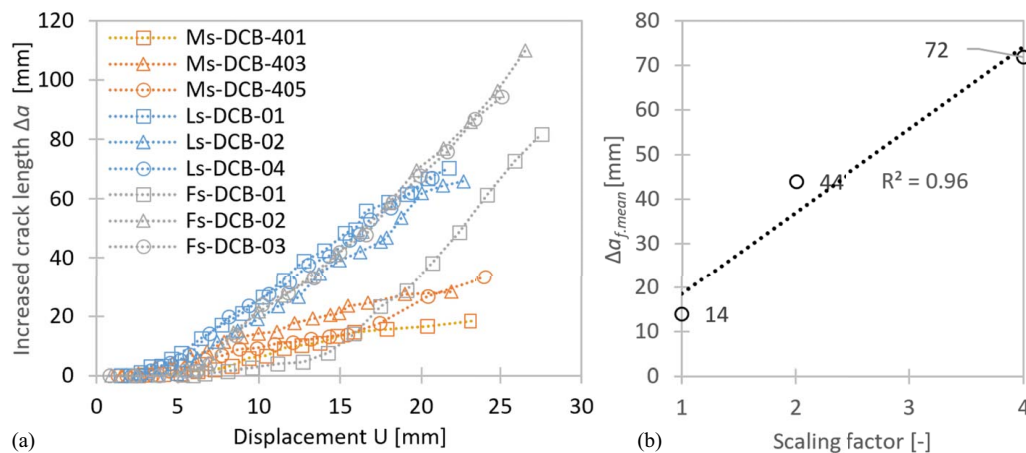

Fig. 7. (a) Increased crack length measured in DCB specimens, including Ms, Ls, and Fs series; and (b) mean value of increased crack length measured at failure points of DCB specimens.
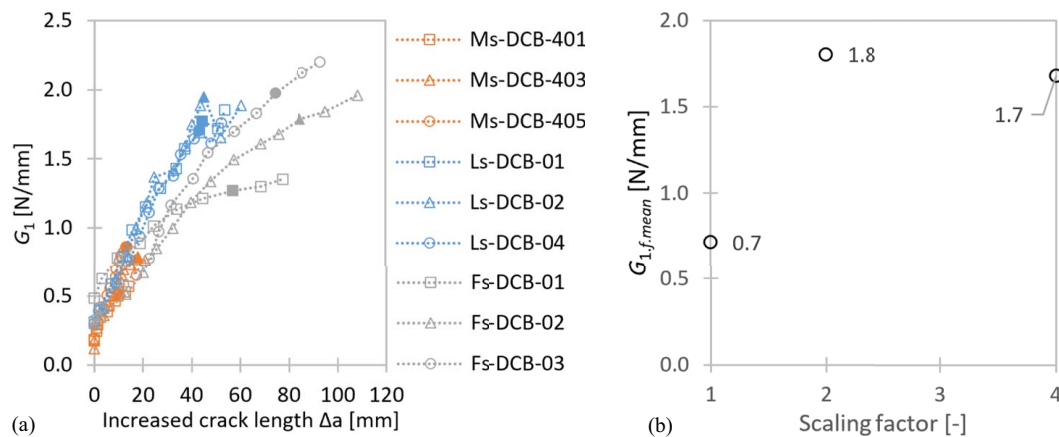
Fig. 8. (a) R-curve in Mode I for Ms, Ls, and Fs specimens; and (b) mean value of G_I measured at failure points of DCB specimens.

By contrast, the average values of G_I at failure points ($G_{I,f.\text{mean}}$) for the Ls and Fs specimens were consistent (1.7–1.8 N/mm), and significantly larger than those observed in the Ms specimens, as shown in Fig. 8(b). The observed variation in SERR for the Ms specimens is attributed not to size effects, but rather to inconsistencies in the bonding conditions of this batch of Ms DCB specimens. This inference for Ms specimens is supported by the observation of significantly fewer fiber bridges in the fracture process zones than in those in the Ls and Fs specimens, as shown in Fig. 9. It is hypothesized that if Ms specimens exhibited a bond quality similar to that of the Ls and Fs specimens, their estimated SERR at the failure point would probably match more closely, showing minimal impact from the scaling factor. Additional testing of more Ms DCB specimens is being conducted to further investigate this hypothesis.

4ENF Tests

Similar to DCB tests, the critical parameters of 4ENF specimens at the failure point are given in Table 5. This table serves as a basis for comparing the specimens across different scales and provides insights into the impact of the scaling factor.
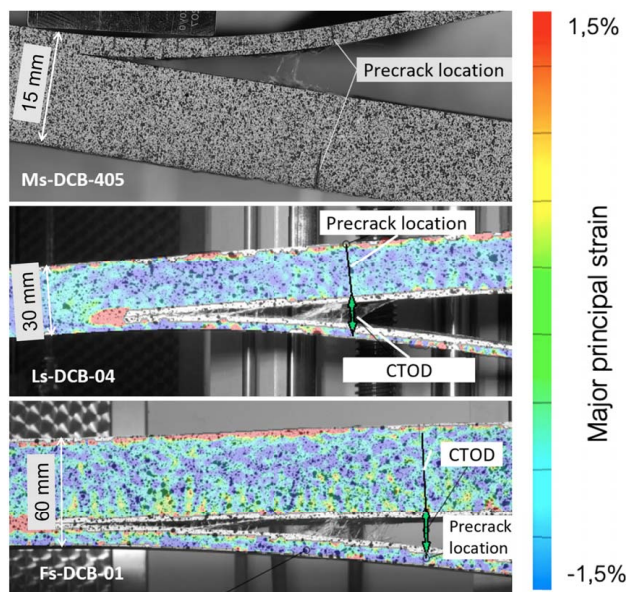

Fig. 9. Fracture process zone in Ms, Ls, and Fs DCB specimens (randomly selected), focusing on fiber bridging.

Load–Displacement

During the 4ENF tests, the displacement of the specimen was calculated as the net displacement between the two loading points and the two supports, based on DIC measurements. Fig. 10(a) illustrates the net displacement against the applied load. As shown in Fig. 10(b), both the displacement and the load at the failure point demonstrate a linear dependency on the scaling factor, exhibiting similar size effects to those observed in the DCB specimens.

CTOD

In the 4ENF tests, the CTOD refers to the in-plane shear slip measured at the precrack tip of the specimens. The CTOD in the 4ENF specimens was determined through the analysis of data acquired by DIC. Fig. 11(a) presents the CTOD for the 4ENF specimens across three scales. Fig. 11(b) displays the mean values of CTOD at the failure point for specimens of different scales. Notably, the mean CTOD values for the Ms and Fs groups are similar, whereas the Ls specimens exhibit a higher CTOD at failure. This discrepancy could be attributed to the better bond quality and greater fracture toughness of the Ls ENF specimens. This is further discussed in the subsection on R-curves in Mode II. When the CTOD in 4ENF specimens reaches 0.4 mm, the higher fracture resistance of the Ls specimens means that it allows more extensive development of the fracture zone and delays the onset of rapid crack growth and the load decrease. Consequently, the failure point in Ls specimens is recorded at a higher CTOD, compared with Ms and Fs specimens. To verify whether the CTOD in 4ENF specimens is

Table 5. Parameters measured at failure point of 4ENF specimens

Scale (−)	Specimen (−)	U_f (mm)	F_f (kN)	$CTOD_f$ (mm)	Δa_f (mm)	G_{IIf} (N/m)
Ms	Ms-4ENF-421	6.42	10.4	0.50	22.4	7.6
	Ms-4ENF-422	6.30	10.2	0.44	20.2	8.4
	Ms-4ENF-423	6.03	10.3	0.32	21.0	8.2
Ls	Ls-4ENF-08	7.51	30.1	0.46	29.3	10.9
	Ls-4ENF-09	7.62	31.4	0.81	58.4	11.6
	Ls-4ENF-10	9.61	31.8	0.78	48.5	11.8
Fs	Fs-4ENF-01	9.80	80.1	0.6	45.7	8.1
	Fs-4ENF-02	10.93	72.5	0.28	36.1	7.3
	Fs-4ENF-04	12.62	87.8	0.4	39.4	10.7

Note: U_f = displacement; F_f = load; $CTOD_f$ = crack-tip opening displacement; Δa_f = increased crack length; and G_{IIf} = strain energy release rate (Mode II), all at the failure point of each 4ENF specimen.
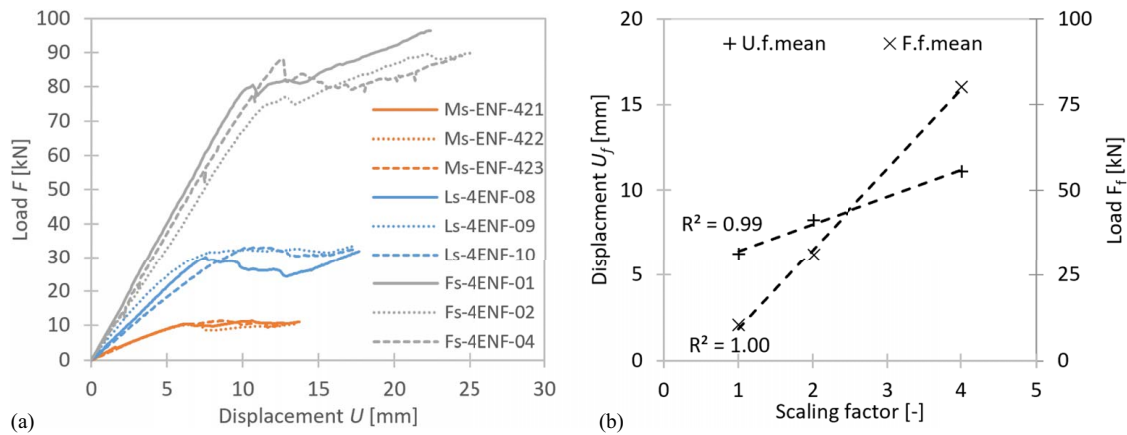
Fig. 10. (a) Load–displacement relationship of 4ENF specimens in Ms, Ls, and Fs series; and (b) mean values of displacement and load measured at failure points of 4ENF specimens.
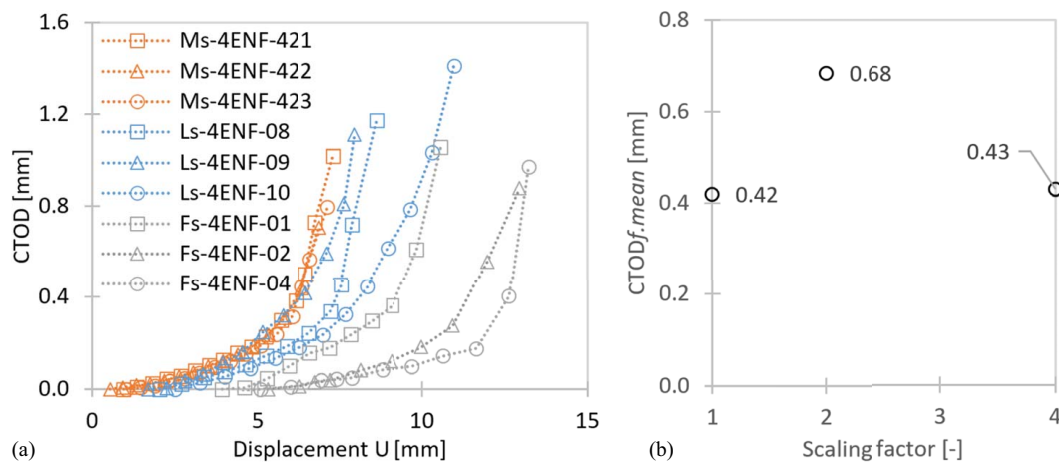

Fig. 11. (a) CTOD of 4ENF specimens in Ms, Ls, and Fs series; and (b) mean value of CTOD measured at failure points of 4ENF specimens.

unaffected by the upscaling of specimen sizes, further testing on more Ls 4ENF specimens with fracture toughness similar to that of Ms and Fs 4ENF specimens is necessary.

Development of Interfacial Cracking

For the specimens in the 4ENF tests, the local deformation of in-plane shear along the bond line was accurately assessed by DIC. Fig. 12 illustrates the approach to identifying the location of the crack tip, based on the shear strain distribution derived along the interface curve and a properly defined threshold.

Based on the DIC data analysis, Fig. 13(a) displays the propagation of interfacial cracks in the 4ENF specimens. The average increased crack length measured at the failure point is detailed in Fig. 13(b). Similar to the observations made for DCB specimens, the increased crack length at the failure point (i.e. the length of the fracture process zone) shows a clear effect from the scaling of specimens. However, owing to the inconsistent bonding conditions, Ls specimens exhibit a disproportionally greater increase in crack length at the failure point, compared with Ms and Fs specimens. To definitively establish the effect of size scaling on interfacial crack growth in Mode II, additional Ls 4ENF specimens, possessing fracture toughnesses comparable to the Ms and Fs specimens, need to be examined.

R-Curves in Mode II by EGM

The SERR in Mode II was evaluated using the EGM (Shahverdi et al. 2014) as

$$G_{II} = \frac{M_{II}^2}{2B(EI)_{eq1}}(1 + \psi - \xi(1 + \psi)^2) \tag{6}$$

with

$$\xi = \frac{(EI)_{eq1}}{(EI)_{eq}} \tag{7}$$

The Mode II R-curves are shown in Fig. 14(a), in relation to the increased interfacial crack length in the 4ENF specimens.

The Ms and Fs 4ENF specimens demonstrate a plateau of G_{II} at approximately 8 N/mm, while the Ls specimens exhibit a distinctly higher plateau range for G_{II} at the failure point, ranging between 11 and 12 N/mm. The mean values of G_{II} at the failure points of each scale of specimens are compared in Fig. 14(b), highlighting noticeable differences in the fracture toughnesses of the Ls specimens. This leads to the distinction in the interfacial parameters of the Ls specimens, compared with the Ms and Fs specimens, as discussed in the previous section on CTOD and increased crack length. To definitively establish whether the values of G_{II} at the
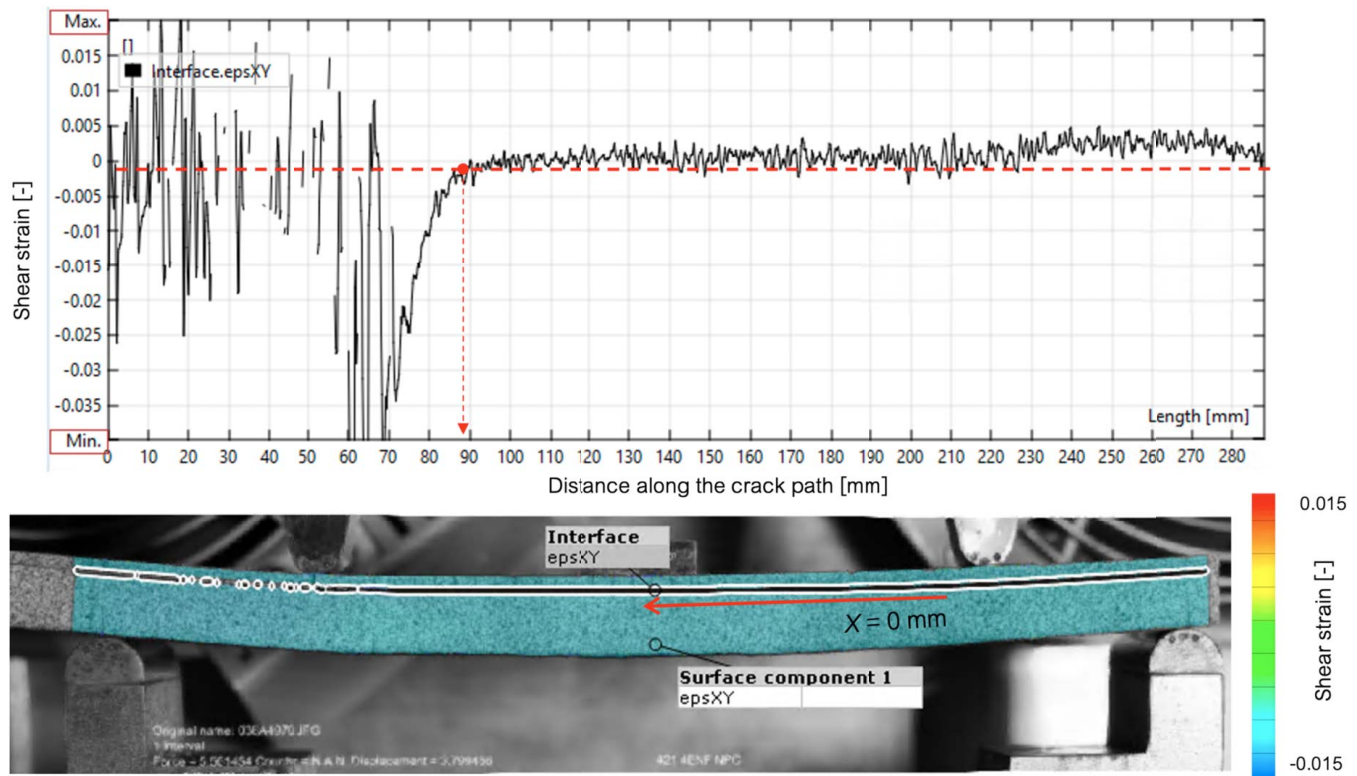
Fig. 12. Identification of location of crack tip in Ms-4ENF specimen based on DIC-acquired data—shear strains are shown as detailed results along the path defined in the DIC image. [Reprinted from Yang et al. (2023), under Creative Commons-BY-4.0 license (https://creativecommons.org /licenses/by/4.0/).]
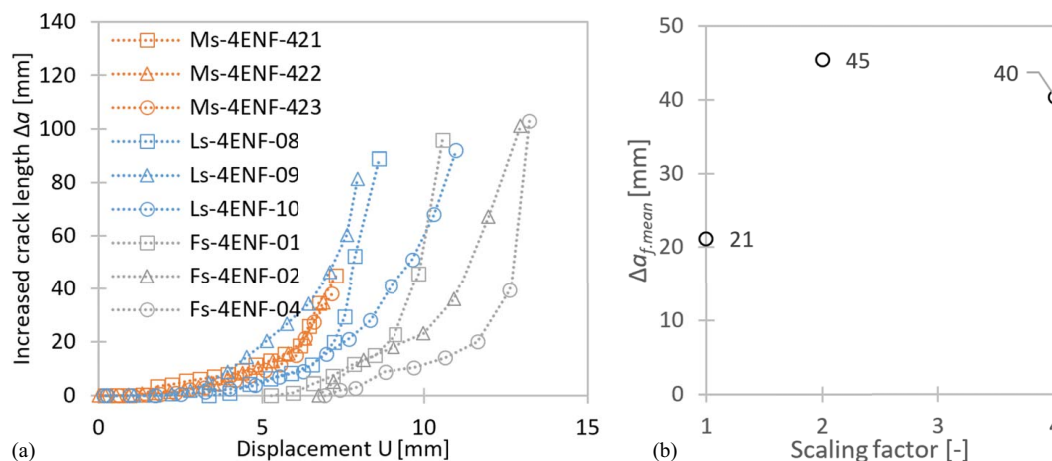

Fig. 13. (a) Increased crack length measured in 4ENF specimens including Ms, Ls, and Fs series; and (b) mean value of increased crack length measured at failure points of 4ENF specimens.

failure point are independent of the scaling size of the 4ENF specimens, additional testing and analyses of Ls specimens are required.

Mode II Traction-Separation Law

For the Mode II cohesive behavior, a four-linear $T–\delta$ law was applied to model the four different stages that describe the Mode II crack development: linear elastic behavior, hardening, maximum traction, and softening. A maximum traction plateau of 25 N/mm^2 was set for the Mode II fracture condition. The critical points required to define the $T–\delta$ relationship were the average values obtained from the midscale 4ENF experiments at the crack onset and crack propagation stages. The traction was extracted

from the average SERR, calculated using the EGM. The separation at rupture (when the traction is equal to 0) was obtained from the average crack slip at the crack propagation stage, measured from DIC. Fig. 15 shows the Mode II cohesive law.

Validation by FEA

Modeling Strategy

Two types of finite-element (FE) model, replicating DCB and ENF experiments, were built and analyzed using the Abaqus software
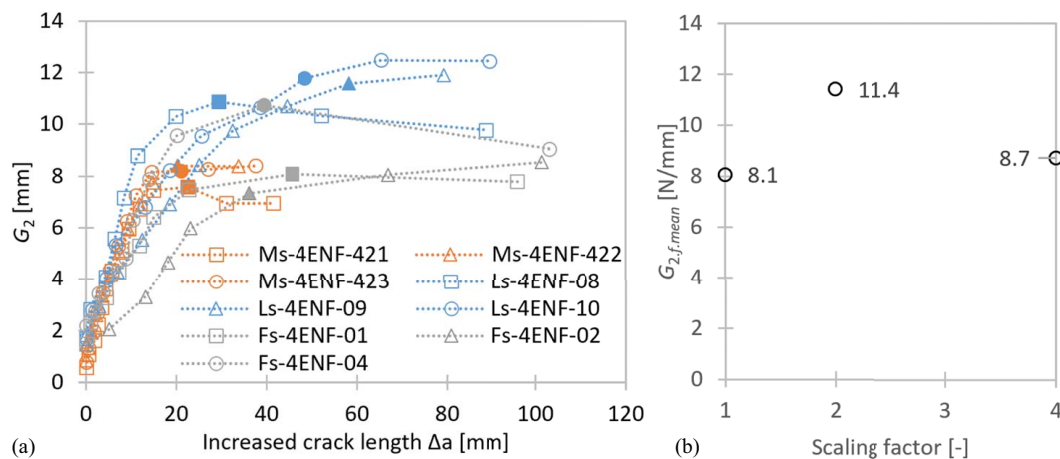
Fig. 14. (a) R-curve in Mode II for Ms, Ls, and Fs specimens; and (b) mean value of G_{II} measured at failure points of 4ENF specimens.
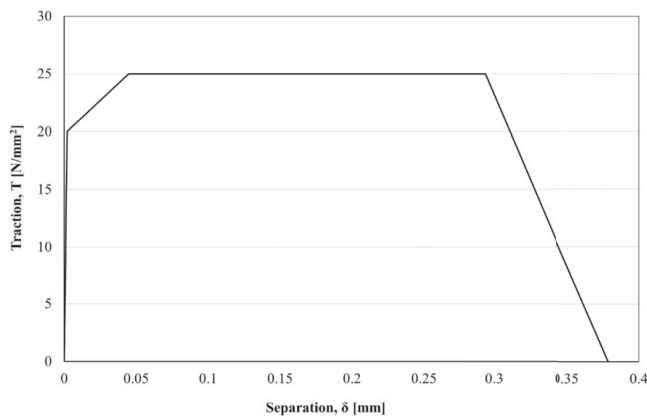

Fig. 15. Mode II traction-separation law.

package: cohesive zone FE models and virtual crack closure technique (VCCT) FE models. In both types of model, variants were constructed at all three different scales and compared with experiments.

The first set of models used CZM applied to an interface interaction between steel and composite parts to model crack initiation and propagation debonding, based on the traction-separation law derived from experiments. Only the Mode II fracture behavior was considered, as this is the dominant fracture mode for composite wrapped joints. The aim of the FE Mode II CZM is to test whether a unique traction-separation law can be used to obtain a good match to ENF experiments across the scales. If successful, the cohesion zone model with such a traction-separation law would be deemed size-independent and could be used for the analysis of debonding size effects in complex bonded FRP–steel joints, such as wrapped composite joints, up to full scale.

The second set of models used the VCCT for several fixed (stationary) cracks to establish the SERR at the crack tip as an alternative to the analytical EGM. The fracture criterion for the VCCT, combined with friction behavior, was defined for the bonded composite-to-steel interface. The Benzeggagh–Kenane mixed-mode criterion was employed to model the fracture behavior. High values of 100 N/mm were used in the analysis for the critical Mode I and Mode II SERRs, instead of the actual values. This was to prevent crack propagation, since the FE model was used to obtain SERRs at a stationary crack tip. Since Mode I is not relevant in this study, the same critical value was defined for the Mode I and Mode II SERRs. The aim was to check the influence of plasticity

in the steel constituent of the bimaterial fracture mechanics tests, as well as the influence of friction at the interface. The latter is only important in the case of Mode II behavior, which is the only behavior that was studied here.

Owing to nonlinearity introduced by steel yielding and friction at the interface, the SERR could be altered, compared with values obtained using the EGM. Models were analyzed for stationary cracks having the original, precrack, length and for steps of extended crack lengths to check and characterize the influence of yielding and friction in such nonlinear systems.

Friction at the interface between the steel and the composite substrate was modeled as an additional definition of hard-contact and penalty-formulated friction behavior, with a coefficient of 0.5, within the same contact interaction property definition in Abaqus software in which the cohesive law was defined. In such a definition, the behaviors arising from the friction formulation and the cohesive formulation act in a decoupled manner. Friction behavior was activated at a point on the interface once the cohesive-law damage was fully developed, that is, friction was only active in the debonded (cracked) portions of the interface, excluding the still-bonded portion and the fracture process zone.

As the result of the analysis, the SERR in Mode II at the crack tip was expressed as a set of nonlinear functions of crack length and applied force in the 4ENF setup and compared with the Mode II SERR obtained using the EGM, where only dependency on load level exists. The goal was to investigate the applicability and accuracy of a well-established EGM on larger-scale fracture mechanics coupons.

Description of FE Model

A commonly used method for determining the SERR at the crack tip involves using FE models by means of the VCCT. Based on the VCCT, a three-dimensional (3D) FE model was built in the explicit solver of Abaqus software, as shown in Fig. 16 (a 4ENF Ms model is shown, as an example). A model was built for all three scales: Ms, Ls, and Fs. The geometry and boundary conditions of the FE models followed the design of the ENF and 4ENF specimens. A four-node linear tetrahedron element type (C3D4) was used for the composite part, while eight-node solid linear hexahedron elements with reduced integration (C3D8R) were used for all steel parts.

Material properties used in the models were the same as presented previously, in the section on material and interface specimens. The steel part was modeled as an isotropic material. The
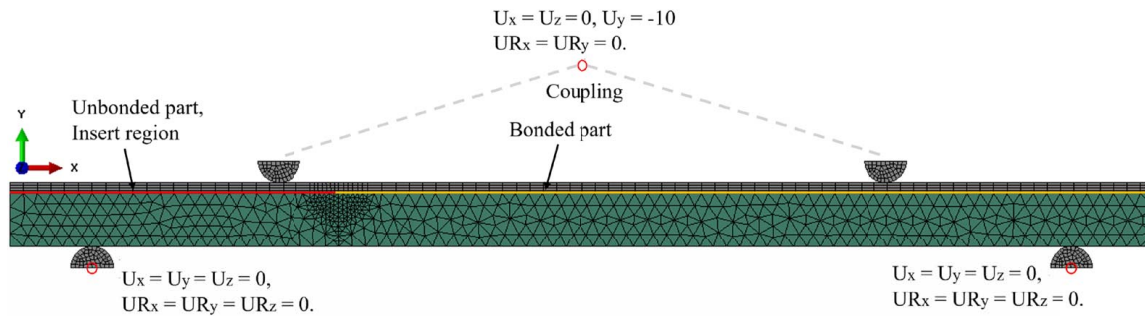
Fig. 16. Boundary conditions and mesh topology of 4ENF VCCT FE model: Ms model as example, with crack length $a = 69$ mm.
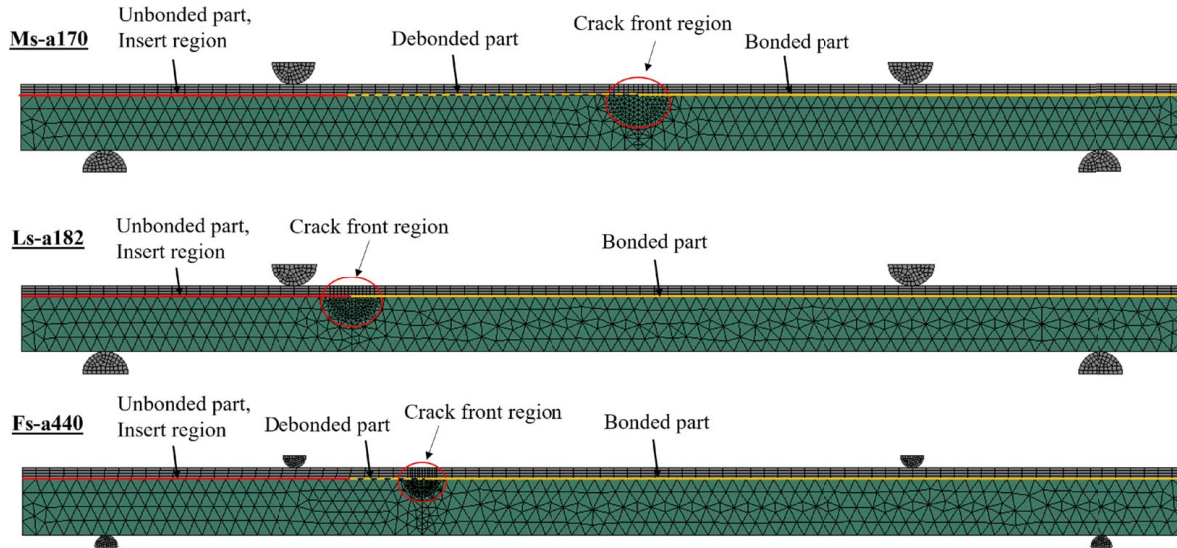

Fig. 17. Mesh topology at three scales, indicating different interface regions.

composite laminate was modeled as a bulk orthotropic material, with elastic properties corresponding to those shown in Table 2.

A 4ENF VCCT model was created for all three size scales, Ms, Ls, and Fs. The mesh topology of the three different scales is shown in Fig. 17; the mesh size used for each model is given in Table 6. Global mesh was used for the steel and composite parts of the specimen, except in the region next to the crack front, where a smaller local mesh size was used. The meshing of the load and support points also differed from the global mesh. Fig. 17 also highlights different parts of the steel–composite interface; this is important for the 4ENF VCCT models that included the effects of friction. The solid line on the left to the zone indicating the crack front region indicates the location of the nonadhesive insert, used to create the precrack in the specimens. The coefficient of friction used at the insert region was $\mu = 0.3$. The dotted line left to the zone indicating the crack front region marks where the composite and steel had become debonded. Six different debonding lengths were analyzed for each scale, and are given in Table 7. The coefficient of friction used at the debonded region was $\mu = 0.5$. The solid

line on the right to the zone indicating the crack front region marks where the composite and steel parts were still intact; thus, no effect of friction was present at the interface in that region.

Mode II Interface Fracture by CZM

In this work, only the Mode II fracture behavior was modeled. A unique traction-separation law, detailed in the section on R-curves in Mode II by EGM, was applied consistently for the Mode II CZM at all scales. The modeling results for CZM simulations of 4ENF experiments across all scales are illustrated in Fig. 18, alongside corresponding experimental data. The 4ENF numerical load–displacement curves exhibit good agreement with experimental data. Both the initial stiffness and the ultimate load are within the range of experimental variations. This suggests a better overall

Table 6. Mesh size of 4ENF VCCT FE models in Ms, Ls, and Fs series

Model series	Global (mm)	Crack front region (mm)	Load point (mm)	Support point (mm)
Ms	3.75	1.25	1.25	1.25
Ls	7.5	1.875	2.5	2.5
Fs	15	2.5	2.5	2.5

Table 7. Mesh size of 4ENF VCCT FE models in Ms, Ls, and Fs series

Crack length (mm)			Ms ($\times 10^{-4}$)		Ls ($\times 10^{-4}$)		Fs ($\times 10^{-4}$)	
Ms	Ls	Fs	C2	C1	C2	C1	C2	C1
69	136	270	748	20	105	−109	13.3	−44.2
72	144	288	776	61	103	−68	12.8	−54.3
77	154	308	742	234	101	−28	12.8	−50.8
87	174	348	648	465	101	−6	12.7	−49.3
107	214	428	592	465	90	146	12.2	−25.7
147	294	588	676	230	69	369	11.2	25.4
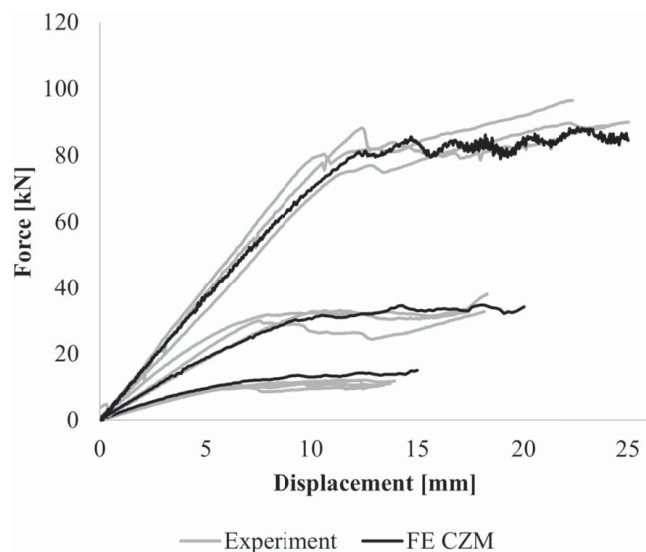
Fig. 18. Load–displacement curves from 4ENF tests: experimental versus FE modeling.

Fig. 19. SERR, Mode II, versus load for 4ENF VCCT versus EGM.

alignment of the numerical and experimental outcomes for the 4ENF test configuration.

From the numerical results obtained using CZM, it can be concluded that the use of a unique traction-separation law, based on the results of medium scale interface tests, across several scales provides a generally good prediction of the fracture behavior, compared with the experimental results. However, it is noted that the interface interaction can be modeled more accurately by accounting for the size effects in the calculation of the SERR in relation to the impact of friction and through-thickness shear stress concentration at the crack front.

Results of SERR Mode II Determined by VCCT

A comparison between the Mode II SERR, at the crack front, computed using the EGM, on the one hand, and the VCCT, on the other, is given in Fig. 19. It shows the nonlinear dependency of the load and the Mode II SERR. The results in Fig. 19 are taken as an example from a Fs 4ENF model with an initial crack length of 270 mm. The same comparison was also computed for both Ms and Ls 4ENF models. In Fig. 20, the Mode II SERR results from FEA are normalized against the Mode II SERR results obtained using the EGM, for all three scales. At the failure load level, marked with a dotted black line, there is a 35% reduction in the Mode II SERR from the EGM, compared with a VCCT model
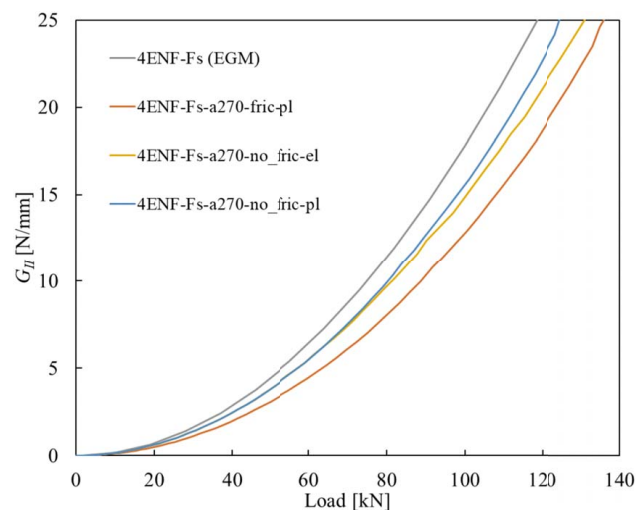
including steel plasticity and interfacial friction at the Ms. When no friction is considered, the decrease is 20%. For the Ls, the corresponding Mode II SERR decreases are 30% (plasticity and friction) and 16% (plasticity only); similarly, for the Fs, the decreases are 30% and 12%. The conclusion is that the decrease in the SERR caused by friction is in the range 17%–19% across all the scales. The large dependency on the plastic behavior of the steel substrate is found by comparing the FEA results and those obtained using the EGM with the data reduction method. Therefore, FEA is recommended for determination of the SERR in such cases over analytical data reduction, e.g., following the EGM.

Fig. 21 shows how the relationship between load and Mode II SERR changes when the crack length at the steel–composite interface increases. Steel plasticity and interfacial friction are included. The results shown in Fig. 21 represent the Fs VCCT model as an example; the same results were also obtained for the Ms and Ls VCCT simulations. The general trend is that the SERR at the crack front reduces for the same load magnitude, for an increased crack length. This is expected, since the surface area where energy is dissipated through frictional effects is expanded for an increased crack length. There is less difference between the data for the shorter crack lengths, since there are smaller jumps in crack length. The Mode II SERR data points for each of the crack lengths were fitted to a second-order polynomial, with F as an independent variable:

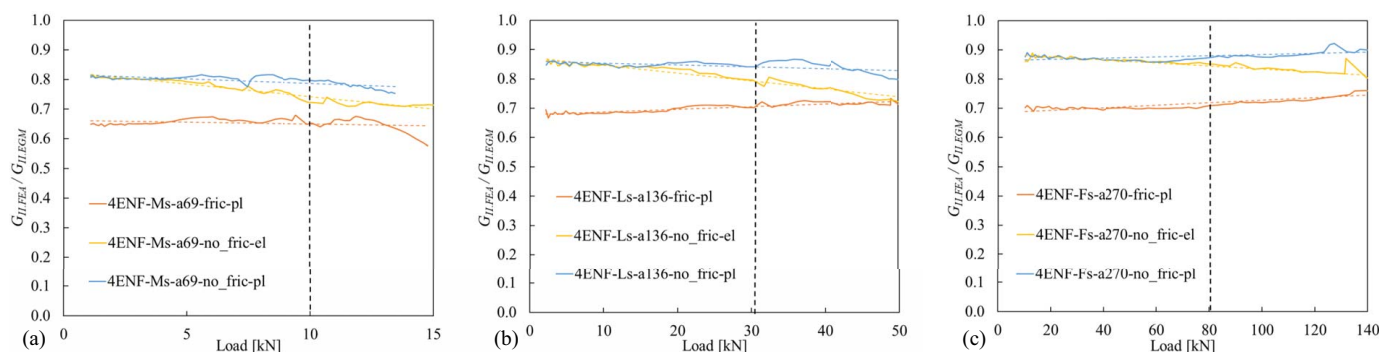$$\text{SERR(F)} = C_2 \cdot F^2 + C_1 \cdot F \tag{8}$$

Fig. 20. Mode II SERR from FEA normalized against Mode II SERR from EGM: (a) medium scale; (b) large scale; and (c) full scale.
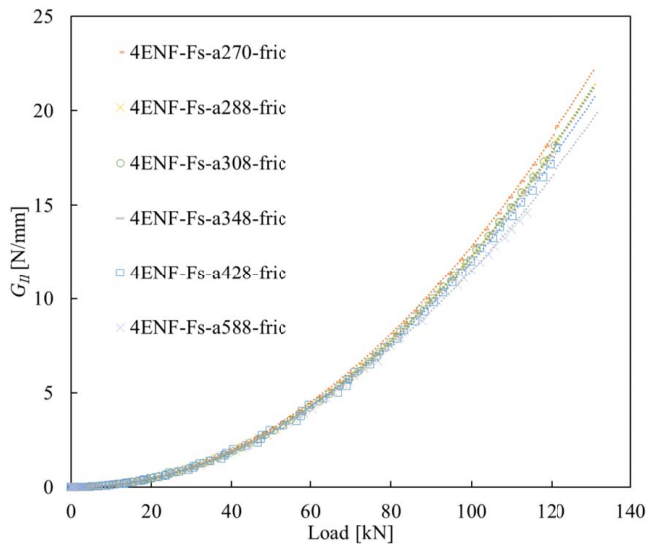
Fig. 21. SERR Mode II as a function of load for several crack lengths at full scale (FS): curve fitting by second-order polynomial.

Fig. 22. Fitting parameters C_1 and C_2 for Fs 4ENF.

The coefficient C_1 is nonzero, owing to the linear effects of friction. The fitting parameters, along with the crack lengths used for the analysis, are given in Table 7 for the Ms, Ls, and Fs series.

When the effects of friction are included, the SERR at the crack front is a function of the load applied, F, and the crack length, a. The form of the equation is

$$\text{SERR}(F, a) = (F^2 \cdot C_2(a) + F \cdot C_1(a)) \times 10^{-4} \qquad (9)$$

However, for all three scales, Ms, Ls, and Fs, the functions of the crack length, $C_2(a)$ and $C_1(a)$, will differ between the scales. If there were no effects of friction, as when the SERR is calculated using the EGM, the SERR would only be a function of the applied load.

The coefficients presented in Table 7 were fitted to a polynomial, to obtain the functions $C_2(a)$ and $C_1(a)$ for all three scales. As an example, Fig. 22 visualizes the fitting curves for the Fs model. The coefficient functions for each scale are

$$C_2(a)_{Fs} = -0.006a + 14.714 \qquad (10)$$

$$C_1(a)_{Fs} = 0.2431a - 123.5 \qquad (11)$$

$$C_2(a)_{Ls} = -0.2264a + 136.94 \qquad (12)$$

$$C_1(a)_{Ls} = 2.9762a - 502.9 \qquad (13)$$

$$C_2(a)_{Ms} = 0.0874a^2 - 20.207a + 1756.5 \qquad (14)$$

$$C_1(a)_{Ms} = -0.2694a^2 + 60.512a - 2854.7 \qquad (15)$$

To obtain a good fit, the Ms coefficients had to be fitted to a second-order polynomial, instead of a first-order polynomial. With the use of the completed functions [SERR(F, a)] for all three scales, R-curves based on the VCCT analysis can be derived.

Fig. 23 shows the normalized through-thickness shear stresses, σ_{13}, at the location of the crack front over the thickness of the composite material, for all three scales. Initial and final crack lengths were examined but no significant difference can be seen based on the crack locations. When the three scales are compared, it can be concluded that the shear stress concentration at the crack front increases when the scale increases.
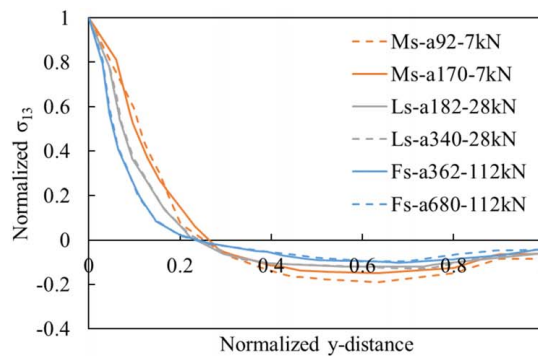

Fig. 23. Normalized through-thickness shear stresses over the normalized thickness of the composite for different scales in a cross section at the crack tip.
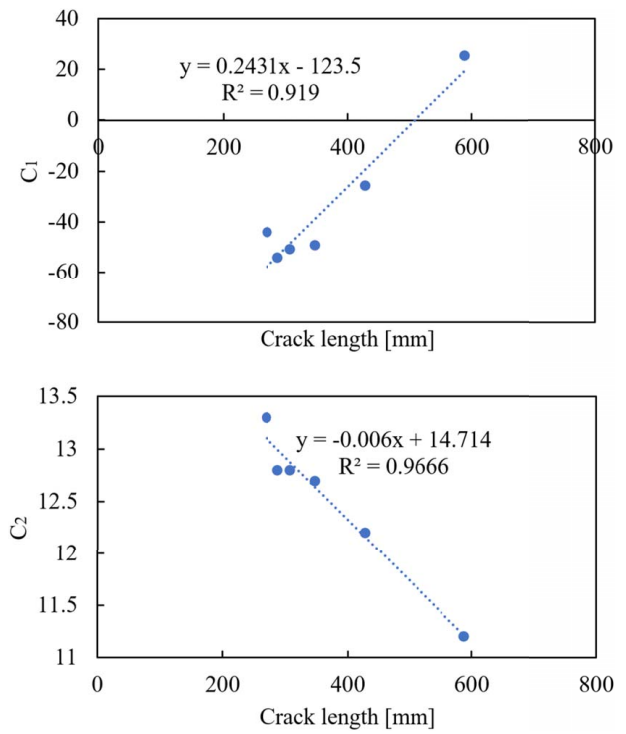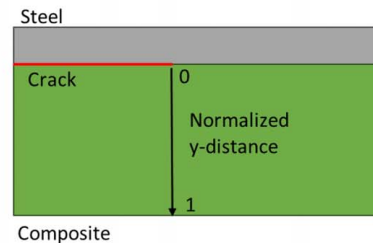
Conclusion

This study was focused on experimental and numerical investigations of fracture properties at FRP–steel interfaces, with a specific emphasis on size effects in both Mode I and Mode II loading conditions. Based on the results of this experimental and numerical study, the following conclusions are drawn.

1. The behavior of bimaterial interface specimens under both Mode I and Mode II conditions in upscaled DCB and 4ENF tests demonstrates that both displacement and load at the failure point exhibit a clear linear dependence on the dimensional scaling of specimens.
2. The fracture toughness, determined from experiments (i.e., the SERR at the critical point), of bimaterial interface specimens reveals minimal size effects in both Mode I and Mode II.
3. The experiments on bimaterial interface specimens, in both Mode I and Mode II, reveal a significant influence of specimen scaling on the length of the fracture process zone measured at the failure point. Additional experiments and FEAs are necessary to determine, explicitly, the relationship between the length of the fracture process zone and the scaling factor.
4. The analysis of CTOD at the interface indicates independency of the CTOD at the failure point in Mode II behavior. This implies that a unique traction-separation law can be used to model Mode II dominated behavior of steel–composite bimaterial bonded joints.
5. Numerical results using unique CZM showed good agreement with experimental results from 4ENF tests across several scales.
6. Frictional effects show a similar impact on 4ENF testing at several scales. An approximately 30%–35% lower SERR is obtained from a VCCT-based numerical analysis at failure load for all scales, incorporating friction at the precrack and the cracked interface, compared with the analytical EGM, which does not account for these effects. Furthermore, the decrease in SERR caused by friction is in the range 17%–19% across all the scales, when comparing results from the FEA. The SERR was found to be dependent on crack length, owing to the increase in frictional effects as the crack grows.

Data Availability Statement

Some or all data, models, or code that support the findings of this study are available from the corresponding author on reasonable request.

Acknowledgments

References

Arouche, M. M., M. N. Saleh, S. Teixeira de Freitas, and S. de Barros. 2021a. "Effect of salt spray ageing on the fracture of composite-to-metal bonded joints." *Int. J. Adhes. Adhes.* 108: 102885. https://doi.org/10.1016/j.ijadhadh.2021.102885.

Arouche, M. M., S. Teixeira de Freitas, and S. de Barros. 2021b. "On the influence of glass fiber mat on the mixed-mode fracture of composite-to-metal bonded joints." *Compos. Struct.* 256: 113109. https://doi.org/10.1016/j.compstruct.2020.113109.

Arouche, M. M., S. Teixeira de Freitas, and S. de Barros. 2022. "Evaluation of the strain-based partitioning method for mixed-mode I+II fracture of bi-material cracks." *J. Adhes.* 98 (6): 577–605. https://doi.org/10.1080/00218464.2021.1981297.

Davidson, B. D., X. Sun, and A. J. Vinciquerra. 2007. "Influences of friction, geometric nonlinearities, and fixture compliance on experimentally observed toughnesses from three and four-point bend end-notched flexure tests." *J. Compos. Mater.* 41 (10): 1177–1196. https://doi.org/10.1177/0021998306067304.

Feng, W., M. M. Arouche, and M. Pavlovic. 2024. "Influence of surface roughness on the mode II fracture toughness and fatigue resistance of bonded composite-to-steel joints." *Constr. Build. Mater.* 411: 134358. https://doi.org/10.1016/j.conbuildmat.2023.134358.

Feng, W., P. He, and M. Pavlovic. 2022. "Combined DIC and FEA method for analysing debonding crack propagation in fatigue experiments on wrapped composite joints." *Compos. Struct.* 297: 115977. https://doi.org/10.1016/j.compstruct.2022.115977.

Feng, W., and M. Pavlovic. 2021. "Fatigue behaviour of non-welded wrapped composite joints for steel hollow sections in axial load experiments." *Eng. Struct.* 249: 113369. https://doi.org/10.1016/j.engstruct.2021.113369.

He, P. 2023. "Debonding resistance of CHS wrapped composite X-joints." Ph.D. thesis, Dept. of Engineering Structures, Delft Univ. of Technology.

He, P., W. Feng, and M. Pavlovic. 2023. "Influence of steel yielding and resin toughness on debonding of wrapped composite joints." *Compos. Struct.* 312: 116862. https://doi.org/10.1016/j.compstruct.2023.116862.

He, P., and M. Pavlovic. 2022. "Failure modes of bonded wrapped composite joints for steel circular hollow sections in ultimate load experiments." *Eng. Struct.* 254: 113799. https://doi.org/10.1016/j.engstruct.2021.113799.

Heidari-Rarani, M., M. M. Shokrieh, and P. P. Camanho. 2013. "Finite element modeling of mode I delamination growth in laminated DCB specimens with R-curve effects." *Composites, Part B* 45 (1): 897–903. https://doi.org/10.1016/j.compositesb.2012.09.051.

Jiang, Z., Z. Fang, S. Wan, and K. Xie. 2021. "Mode-II fracture behavior evaluation for adhesively bonded pultruded GFRP/steel joint using four-point bending test." *Thin-Walled Struct.* 167: 108130. https://doi.org/10.1016/j.tws.2021.108130.

Ouyang, Z., and G. Li. 2009. "Nonlinear interface shear fracture of end notched flexure specimens." *Int. J. Solids Struct.* 46 (13): 2659–2668. https://doi.org/10.1016/j.ijsolstr.2009.02.011.

Schuecker, C., and B. D. Davidson. 2000. "Evaluation of the accuracy of the four-point bend end-notched flexure test for mode II delamination toughness determination." *Compos. Sci. Technol.* 60 (11): 2137–2146. https://doi.org/10.1016/S0266-3538(00)00113-5.

Shahverdi, M., A. P. Vassilopoulos, and T. Keller. 2014. "Mixed-Mode I/II fracture behavior of asymmetric adhesively-bonded pultruded composite joints." *Eng. Fract. Mech.* 115: 43–59. https://doi.org/10.1016/j.engfracmech.2013.11.014.

Wang, W., R. Lopes Fernandes, S. Teixeira De Freitas, D. Zarouchas, and R. Benedictus. 2018. "How pure mode I can be obtained in bi-material bonded DCB joints: A longitudinal strain-based criterion." *Composites, Part B* 153: 137–148. https://doi.org/10.1016/j.compositesb.2018.07.033.

Williams, J. G. 1988. "On the calculation of energy release rates for cracked laminates." *Int. J. Fract.* 36 (2): 101–119. https://doi.org/10.1007/BF00017790.

Yang, J., M. M. Arouche, S. Egilsson, M. Koetsier, T. Peeters, and M. Pavlovic. 2023. "Size effects on Mode I and Mode II fracture behaviour of composite–steel bonded interface." In *Proc., 11th Int. Conf. on Fiber-Reinforced Polymer (FRP) Composites in Civil Engineering*, 1–10. Geneve, Switzerland: Zenodo.